Materials Today Bio 23 (2023) 100872

Contents lists available at ScienceDirect

Materials Today Bio

journal homepage: www.journals.elsevier.com/materials-today-bio

Enhancing bone tissue engineering with 3D-Printed polycaprolactone scaffolds integrated with tragacanth gum/bioactive glass

Mahsa Janmohammadi [a], Mohammad Sadegh Nourbakhsh [b,*], Marjan Bahraminasab [c,d,**], Lobat Tayebi [e]

[a] Department of Biomedical Engineering, Faculty of New Sciences and Technologies, Semnan University, Semnan, Iran
[b] Faculty of Materials and Metallurgical Engineering, Semnan University, Semnan, Iran
[c] Department of Tissue Engineering and Applied Cell Sciences, School of Medicine, Semnan University of Medical Sciences, Semnan, Iran
[d] Nervous System Stem Cells Research Center, Semnan University of Medical Sciences, Semnan, 3513138111, Iran
[e] Marquette University School of Dentistry, Milwaukee, WI, 53233, USA

ARTICLE INFO

Keywords:
Framework
Guest component
Multi-compartment scaffold
3D models
Bone

ABSTRACT

Tissue-engineered bone substitutes, characterized by favorable physicochemical, mechanical, and biological properties, present a promising alternative for addressing bone defects. In this study, we employed an innovative 3D host-guest scaffold model, where the host component served as a mechanical support, while the guest component facilitated osteogenic effects. More specifically, we fabricated a triangular porous polycaprolactone framework (host) using advanced 3D printing techniques, and subsequently filled the framework's pores with tragacanth gum-45S5 bioactive glass as the guest component. Comprehensive assessments were conducted to evaluate the physical, mechanical, and biological properties of the designed scaffolds. Remarkably, successful integration of the guest component within the framework was achieved, resulting in enhanced bioactivity and increased strength. Our findings demonstrated that the scaffolds exhibited ion release (Si, Ca, and P), surface apatite formation, and biodegradation. Additionally, in vitro cell culture assays revealed that the scaffolds demonstrated significant improvements in cell viability, proliferation, and attachment. Significantly, the multi-compartment scaffolds exhibited remarkable osteogenic properties, indicated by a substantial increase in the expression of osteopontin, osteocalcin, and matrix deposition. Based on our results, the framework provided robust mechanical support during the new bone formation process, while the guest component matrix created a conducive micro-environment for cellular adhesion, osteogenic functionality, and matrix production. These multi-compartment scaffolds hold great potential as a viable alternative to autografts and offer promising clinical applications for bone defect repair in the future.

1. Introduction

Bone defects present a significant and enduring challenge in the field of clinical orthopedic surgery, arising from a variety of causes such as severe trauma, tumor resection, infection, or even the presence of congenital anomalies. These conditions necessitate effective treatment strategies that can address the complex nature of bone repair and regeneration [1]. The conventional approaches for repairing bone injuries, such as autografts (considered the gold standard), allografts, and xenografts, are accompanied by certain limitations. Autografts are constrained by the scarcity of available bone tissue and the potential for donor site morbidity. Allografts and xenografts, on the other hand, are associated with challenges related to immune-mediated rejection and the inherent risk of disease transmission. These drawbacks highlight the urgent need for alternative treatments that can overcome these limitations and provide more effective solutions for bone repair [2]. Tissue-engineered bone substitutes offer a promising solution to overcome the aforementioned limitations by integrating innovative biomaterials, cells, and signaling factors. This novel approach has emerged as a highly viable strategy for addressing the scarcity of available bone tissue and effectively regenerating critically sized bone defects. In particular, the successful healing and regeneration of bone using graft

* Corresponding author. Semnan University, Semnan, P.O.Box 3513119111, Iran.
** Corresponding author. Semnan University of Medical Sciences, Semnan, P.O.Box 3513138111, Iran.
E-mail addresses: s_nourbakhsh@semnan.ac.ir (M.S. Nourbakhsh), m.bahraminasab@semums.ac.ir (M. Bahraminasab).

https://doi.org/10.1016/j.mtbio.2023.100872
Received 28 June 2023; Received in revised form 26 October 2023; Accepted 15 November 2023
Available online 20 November 2023

substitutes necessitates the utilization of materials and processes that optimize osseointegration. By incorporating advanced techniques and tailored biomaterials, tissue-engineered bone substitutes have the potential to revolutionize bone repair and provide improved outcomes for patients in need of critical bone defect regeneration [3,4].

For bone graft substitutes, several key factors are crucial to consider. Firstly, it is essential that these substitutes align with the architecture of the recipient site, ensuring a proper fit and promoting successful integration. Moreover, they should exhibit adequate porosity to facilitate bone growth and possess mechanical properties that closely resemble those of the surrounding native bone. Additionally, cytocompatibility and biocompatibility are vital to ensure a favorable interaction between the substitute and the host tissue. Furthermore, the substitutes should demonstrate biodegradability, allowing for the gradual replacement by new bone tissue over time. Osteoconductivity, which refers to the ability to guide and support new bone formation, is also a critical attribute. Lastly, the substitutes should exhibit osteoinductivity, meaning they can induce and stimulate the differentiation of precursor cells into bone-forming cells, further enhancing bone regeneration. By fulfilling these requirements, bone graft substitutes have the potential to effectively address bone defects and facilitate successful bone repair [5,6].

Three-dimensional (3D) printing has emerged as a highly promising technique for the production of bone graft substitutes. By leveraging this technology, customizable structures can be created, closely mimicking the intricate internal architecture of bones as well as their mechanical properties. This advancement holds immense potential in promoting cellular growth, facilitating cell differentiation, and providing mechano-inductive cues, ultimately leading to effective bone remodeling. The ability of 3D printing to precisely fabricate complex scaffolds with patient-specific designs revolutionizes the field of bone tissue engineering. These scaffolds can provide a supportive platform that matches the unique anatomical requirements of the recipient site, promoting optimal cellular adhesion, proliferation, and differentiation. The customizable nature of 3D-printed bone graft substitutes allows for tailored mechanical properties, ensuring a close match to the surrounding native bone and facilitating successful integration. By harnessing the capabilities of 3D printing, bone graft substitutes can be engineered to deliver mechano-inductive signals to cells, stimulating their response and guiding them towards osteogenic differentiation. This remarkable advancement paves the way for enhanced bone regeneration and remodeling, offering a transformative solution for the treatment of bone defects and facilitating the restoration of functional bone tissue in patients [7,8].

Currently, there exists a diverse range of materials that can be utilized for fabricating bone graft substitutes through the application of 3D printing techniques. Among these materials, polycaprolactone (PCL) scaffolds in their 3D printed form have garnered significant attention and have been extensively employed in both preclinical and clinical settings. However, despite the immense potential of PCL scaffolds, their utility is constrained by certain limitations, both in vitro and in vivo. In vitro, PCL scaffolds often face challenges due to their inherent lack of an active surface that facilitates favorable interactions with cells. This deficiency can hinder optimal cell attachment, proliferation, and differentiation, thereby impeding the desired biological responses within the scaffold. Similarly, in vivo implantation of PCL scaffolds can be limited by the risk of fibrosis encapsulation, wherein the scaffold becomes encased in fibrous tissue, impeding its integration with the surrounding native tissue. This phenomenon prevents the desired tissue regeneration and functional recovery. Addressing these limitations is crucial to unlock the full potential of PCL scaffolds. Strategies aimed at enhancing the bioactivity of PCL surfaces through surface modifications or incorporating bioactive molecules can promote improved cellular responses, fostering enhanced cell adhesion, proliferation, and differentiation within the scaffold. Additionally, innovative approaches to mitigate fibrosis encapsulation, such as incorporating anti-fibrotic agents or incorporating strategies to promote tissue integration, hold promise in enhancing the in vivo performance of PCL scaffolds. By overcoming these challenges, the utility of PCL scaffolds can be significantly expanded, allowing for more successful in vitro and in vivo applications. This progress will contribute to the advancement of 3D printing technologies in bone tissue engineering and pave the way for more effective bone graft substitutes with enhanced biocompatibility and regenerative capabilities [9,10].

To overcome these challenges, one viable approach is the utilization of surface modifications, such as alkaline hydrolysis with sodium hydroxide. This technique enables surface chemistry alterations, resulting in improved surface properties, enhanced hydrophilicity, and increased cellular activity. By employing alkaline hydrolysis, the surface of the scaffold can be rendered more favorable for cell attachment, proliferation, and differentiation, thereby promoting superior integration with the host bone tissue. The process of alkaline hydrolysis involves treating the scaffold with sodium hydroxide, which induces chemical changes on the surface. This treatment enhances the hydrophilic nature of the scaffold, allowing for improved interactions with cells and facilitating the exchange of nutrients and waste products. The altered surface chemistry promotes the formation of a bioactive interface that promotes cellular adhesion and initiates signaling cascades necessary for cell activity and tissue regeneration. By implementing surface modifications through alkaline hydrolysis, the limitations associated with poor cell interaction and integration can be effectively addressed. The modified scaffold surface facilitates a more favorable microenvironment for cellular responses and promotes a seamless integration with the host bone tissue. This approach holds significant potential in enhancing the overall performance and efficacy of bone graft substitutes, paving the way for improved outcomes in bone tissue engineering and regeneration [11]. Our previous study prepared the 3D-printed PCL scaffolds successfully modified by sodium hydroxide. It is reasonable that the 3D-printed PCL scaffolds with surface roughness, porosity, interconnectivity, mechanical properties like those of cancellous bone, bioactivity close to hydroxyapatite, cell viability, and biomineralization could promise bone implants undergoing subsequent treatment [12].

Obviously, coating or incorporating bioactive materials into PCL scaffolds has been widely explored to improve osseous integration, in vitro osteoblast differentiation, and in vivo bone formation. Among the bioactive materials, 45S5 bioactive glass (BG) has been extensively used for bone tissue engineering applications due to its superior osteoconductivity and osteoinductivity, biodegradability, stimulatory effect on osteoblast cell activity, and ion release during the degradation process. More importantly, the incorporation of bioactive materials should significantly increase bone tissue integration. Moreover, the presence of a polymer matrix compared to pure bio-ceramic should lead to improved integration between the implant and bone [13,14]. From the perspective to create biomimetic bone tissue, bioactive phase-reinforced polymer is a preferred material for bone tissue repair and reconstruction. This is because the native bone matrix is a composite mainly made up of collagen reinforced by biological apatite nanoparticles [15]. In analogy with collagen, tragacanth gum (TG), an anionic natural gum, highly branched heterogeneous polysaccharide obtained from the Astragalus genus exudates, has been informed as a novel osteogenic biomaterial. TG consists of water-soluble (tragacanthin) and water-swellable (bassorin) fractions and the abundant hydroxyl (OH) and carboxyl (COOH) groups. The TG structure facilitates intermolecular hydrogen bonding with other molecules and cross-linking [16]. Owing to their remarkable properties, TG has been applied in biomedical applications, especially bone repair, due to desirable biocompatibility, biodegradability, nontoxicity, and allergenic effects on the human body [17]. In principle, by combining bioactive glass with tragacanth gum, matrix properties can be adjusted with chemical composition, and biological and mechanical properties closer to native bone. Thus, the TG-BG matrix meets the need for a structural support component while also improving the biological properties of scaffolds when integrated into a polymer framework, such as PCL.

In this study, we introduced a novel 3D host-guest scaffold model designed to address the complex requirements of bone tissue engineering. The concept involved incorporating a polymeric host component to provide crucial mechanical support, while the guest component was responsible for introducing osteogenic effects. To achieve this, we employed a customized PCL framework as the host, fabricated using advanced 3D printing techniques. The framework was carefully designed to possess the necessary structural integrity and long-term stability, gradually degrading over time to support the formation of new bone. To enhance the bioactivity and cellular response, the pores of the framework were filled with guest components consisting of freeze-dried TG-BG. This combination facilitated improved bioactivity, cell growth, and created an environment conducive to bone tissue development. The guest components were formulated to degrade at a faster rate, creating additional space for bone tissue ingrowth and remodeling. Comprehensive characterizations were conducted to assess the physical, chemical, and mechanical properties of these multi-compartment scaffolds, thereby validating their potential for bone tissue engineering applications. Additionally, the biological properties of the scaffolds were evaluated through in vitro studies, specifically investigating their ability to support cell adhesion, growth, proliferation, and differentiation using MC3T3-E1 cells. The ultimate goal of this research was to develop a controlled multi-compartment scaffold with optimized structure and properties for effective bone regeneration. By harnessing the unique advantages of the host-guest scaffold model and carefully engineering the framework and guest components, we aimed to contribute to the advancement of bone tissue engineering and offer innovative solutions for bone regeneration applications.

2. Materials and methods

2.1. Host fabrication and functionalization

PCL (Sigma-Aldrich, Mn: 80,000) frameworks were fabricated using an Abtin Teb bioprinting machine (Abtin Teb company, Iran) at 90 °C with a strut diameter of 400 μm, the pore size of 700 μm, and a 0−60−120° lay-down pattern. Triangle-shaped PCL frameworks of 20 mm (diameter) × 2 mm (height) were fabricated, cleansed with 70 % ethanol for 15 min, and then cut into discs of 5 mm diameter. The PCL framework was immersed in 1 M NaOH solution (Sigma-Aldrich) for 6 h at a shaking speed of 80 rpm, then the surface modified PCL (M-PCL) were rinsed with deionized water and dried in an oven at 37 °C for the subsequent experiments.

2.2. Extraction of the soluble component of TG

Briefly, 2 % w/v of the crude TG (from the Astragalus bushes stems, Iran) suspension was prepared in Milli-Q water and stirred at 37 °C for 24 h. Then, the solution was centrifuged at 10000 rpm for 20 min, and the supernatant was stored at −20 °C. In order to obtain a clear powder,

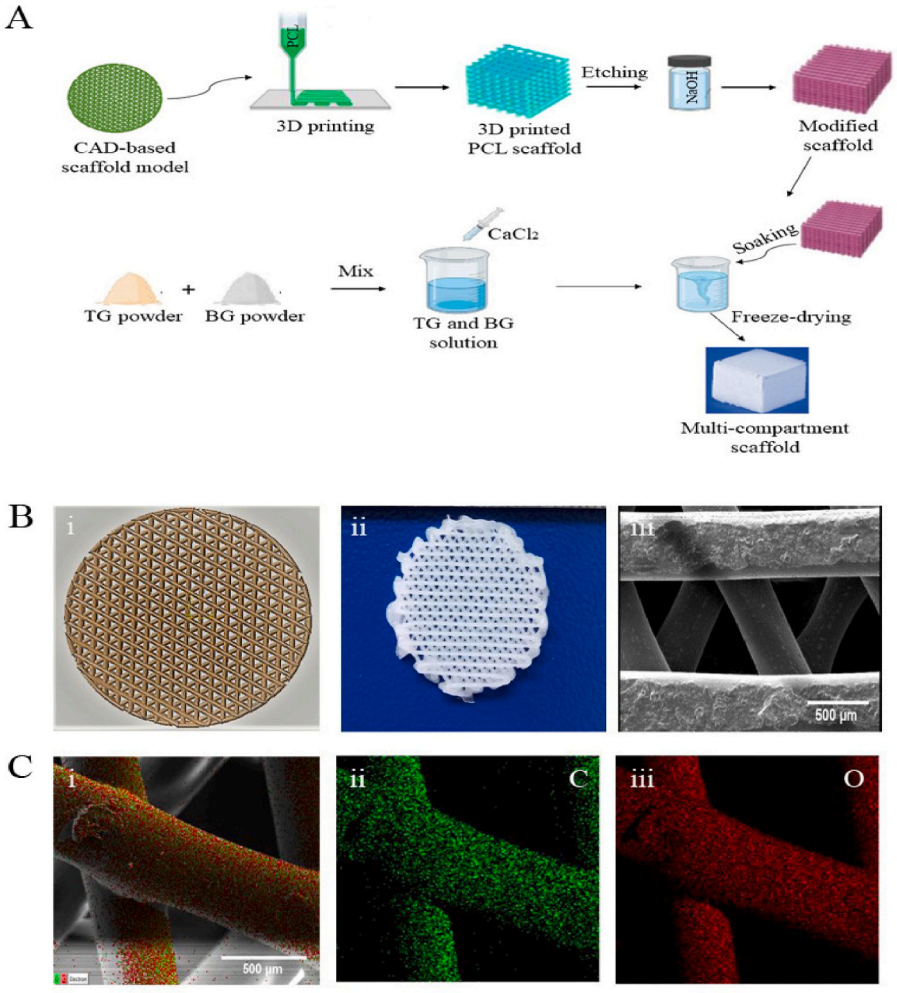

Fig. 1. A) Schematic of multi-compartment scaffold fabrication. B) Host component fabrication (i) CAD-based model, (ii) 3D printed host component, (iii) SEM image of host component (scale bar: 500 μm). C) EDS mapping analysis of the host component (i) EDS mapping in the region of interest (scale bar: 500 μm), (ii) Distribution of chemical composition for C, (iii) Distribution of chemical composition for O.

the frozen soluble part of TG was lyophilized using a freeze-dryer device (Freeze-dryer, Beta plus, Gazlinteb) for 24 h.

2.3. Preparation of host-guest constructs

Multi-compartment scaffolds were fabricated by impregnating the M-PCL scaffold in the TG-BG solution. The 2 % w/v TG powder was first added to deionized water under stirring at 37 °C for 2 h to acquire a homogeneous solution. Then, various amounts of BG (average size of <100 nm, Nik Ceram Razi Co, Iran) including 10, 20, and 30 w/v % were gradually added to the aforementioned sol, and a homogenous polymer/glass hybrid mixture was obtained after 1 h. Afterward, 1.5 % w/v of CaCl2 was added drop-wise into the TG-BG solutions and stirred for 1 h. The M-PCL framework was placed into the TG-BG solutions to obtain the M-PCL/TG-BG constructs. Subsequently, the scaffolds were frozen at −20 °C for 24 h and lyophilized for 24 h in a freeze-dryer (Fig. 1A). Multi-compartment scaffolds were coded as M-PCL/TG-BG10, M-PCL/TG-BG20, and M-PCL/TG-BG30.

2.4. SEM, FTIR and XRD analyses

The surface morphology and cross-section images of the M-PCL frameworks were observed by scanning electron microscopy (SEM, Philips XL30 SEM, Philips, The Netherlands). The scaffolds were gold-coated to make the surfaces conductive for SEM observation. Field-emission scanning electron microscopy (FE-SEM, ZEISS, Germany) and Energy-dispersive X-ray spectroscopy (EDS, ZEISS, Germany) was carried out to evaluate the surface morphology, cross-section images and elemental composition of the multi-compartment scaffolds. X-ray diffraction (XRD, Buker model, D8-Advance USA) of the scaffolds was carried out at a wavelength of 0.154 nm at 40 kV with Cu Kα radiation. Fourier Transform Infrared Spectroscopy (FTIR, Perkin elmer, USA) was performed in the absorption mode in the range 4000–400 cm^{-1} to characterize the functional groups and interactions occurred in the multi-compartment scaffolds.

2.5. Pore size and porosity

The M-PCL, M-PCL/TG-BG10, M-PCL/TG-BG20, and M-PCL/TG-BG30 scaffold pore sizes were measured by ImageJ using SEM images. The porosity of scaffolds was calculated by estimating the porous and non-porous scaffold densities according to eq (1). The porous scaffold density was obtained by measuring the weight and volumes of the scaffolds.

$$p_T = v_{PCL}p_{PCL} + v_{TG}p_{TG} + v_{BG}p_{BG} \quad (1)$$

$$p_M = \frac{m}{\pi r^2 h}$$

$$P\% = (1 - \frac{\rho_M}{\rho_T}) \times 100$$

The p_T and p_M are the theory density, and the measured density of scaffolds, respectively. The densities of PCL, TG, and BG were considered to be 1.145 g/cm^{-3}, 1.25–1.384 g/cm^{-3}, and 2.7 g/cm^{-3}.

2.6. Apatite mineralization on the scaffolds in SBF

The in vitro bioactivity of the scaffolds was assessed in simulated body fluids (SBF) solution. Scaffolds were immersed in ($V_{SBF} = \frac{S_{Sample}}{10}$) of SBF solution at 37 °C for 7 and 14 days. At scheduled time intervals, the scaffolds were collected, washed with distilled water, and dried in an oven at 50 °C. The mineralized apatite on scaffold surfaces was examined by FE-SEM and EDS, and the hydroxyapatite formation was further evaluated by FTIR and XRD. The ion concentrations (Si, Ca, and P) of the solutions were determined by ICP-OES (Cecil, UK) after soaking of the scaffolds for different times. During the soaking time, the solution pH changes were also measured by a pH meter (SAT.CO, Iran).

2.7. Degradation of scaffolds in SBF

The in vitro degradability of the scaffolds was assessed by weight measurements before and after soaking into the SBF solution for up to 28 days, and the degradation ratio of scaffolds was recorded according to eq (2):

$$Degradation\ ratio(\%) = \frac{w_0 - w_t}{w_0} \times 100 \quad (2)$$

where w_o represents the weight of the scaffolds before soaking and w_t represents the scaffold's weight after soaking at different time intervals.

2.8. Mechanical property test

Compression tests were carried out to assess the mechanical properties using a Universal Testing Machine (Instron Ltd., High Wycombe, UK) with a 5 KN load cell. Scaffolds (n = 3) with a diameter and height of 5 mm (aspect ratio of 1) were compressed at a loading rate of 0.03 mm/min to a strain level of 70 %. The stress−strain (σ−ε) curves of the scaffolds were recorded, and the compressive modulus was calculated as the slope of the initial linear stage of the curves.

2.9. Biological assessments

2.9.1. Scaffold sterilization

The scaffolds (3 scaffolds from each group) were sterilized using 70 % ethanol. The scaffolds were taken into Petri dishes, and this procedure was conducted under a laminar flow bench. Then, the scaffolds were UV irradiated for 20 min on each side.

2.9.2. Cell culture and scaffold medium extract

Pre-osteoblast MC3T3-E1 cell line (Mouse C57BL/6 calvaria, ECACC, Sigma-Aldrich, Sweden) was cultured in the growth medium (Dulbecco's Modified Eagle's medium, DMEM, Gibco Life Technologies; USA), 10 % fetal bovine serum (FBS, Gibco Life Technologies; USA), penicillin (100 IU), and streptomycin (100 μg/mL), and 2 mM l-glutamine (Gibco Life Technologies; USA). The cells were incubated at 37 °C in a humidified atmosphere of 5 % CO_2 and 95 % humidity.

To provide scaffold medium extracts, the sterilized scaffolds (n = 3) were placed in 24-well plates and incubated in a complete growth medium of DMEM (2.5 mL per well) for 3 days at 37 °C in a humidified atmosphere containing 5 % CO_2 and 95 % humidity. After 3 days, the scaffolds were discarded and the extract media were used for cellular tests.

2.9.3. Cell viability test

The viability of the cells was measured by a lactate dehydrogenase (LDH) cytotoxicity detection kit (Roche Applied Science, Germany). MC3T3-E1 cells were seeded in 96-well plates at a density of 5×10^3 cells/well to make a monolayer within 24 h. Then, the complete medium was exchanged with the scaffold extract media. Following the incubation for 1, 3, and 7 days, the cells in high control wells were lysed with Triton X100 (100 μL/well) and the plates were centrifuged (250 g for 10 min) and the supernatants were transferred to another 96-well ELISA plate. The LDH mixed detection kit reagent (100 μL/well) was inserted and after 30 min of incubation at room temperature, the absorbance was measured using a microplate ELISA reader (490 nm, Synergy H1 Hybrid Multi-Mode Microplate Reader, BioTek, USA). The cell viability percentage was calculated by eqs (3) and (4).

$$Cytotoxity(\%) = \frac{experiment\ value - low\ control}{high\ control - low\ control} \times 100 \quad (3)$$

$$Viability(\%) = 100 - cytotoxicity \quad (4)$$

In this test, low control was prepared by mixing the supernatants of the cells cultured without scaffolds media with LDH detection mixture, and high control was provided through the maximal LDH activity by lysing the cells using Triton-X100 provided by the kit.

2.9.4. Cell proliferation

Cell proliferation of the cells exposed to scaffolds was evaluated by MTT cell proliferation kit [3-(4,5-dimethylthiazol-2-yl)-2,5- diphenyltetrazolium bromide, Cell Growth Determination Kit, Sigma Life Science) after 1, 3 and 7 days. For cell proliferation, MC3T3-E1 cells (5 × 103 cells/well) were seeded in 96-well plates to make a monolayer within 24 h. Afterward, the complete medium was exchanged with the scaffold media (extracts). After the incubation time (for 1, 3, and 7 days), the medium was replaced with 100 μL incomplete medium, and 10 μL MTT solution (per well). The cells were incubated for 4 h at 37 °C. Finally, isopropanol/hydrochloric acid (100 μL/well, 0.04 N) was added and mixed thoroughly to dissolve the formazan, and the absorbance was assessed using a microplate ELISA reader (570 nm, Synergy H1 Hybrid Multi-Mode Microplate Reader, BioTek, USA).

2.9.5. Osteocalcin evaluation

For Osteocalcin (OCN) evaluation, MC3T3-E1 at a density of 5×10^3 cells/well were seeded to make a monolayer within 24 h. Next, the complete medium was exchanged with the scaffold media and incubated for 7 days. After 7 days, the osteocalcin level of cells was also evaluated in the supernatant, using a sandwich ELISA method (Rat Osteocalcin/Bone Gamma-Carboxyglutamic Acid Containing Protein (OT/BGLAP) EISA Kit; ZellBio, Germany) according to the manufacturer's instruction.

2.9.6. Cell density and distribution

To further examine the cell viability, phalloidin-fluorescein isothiocyanate (FITC) solution (Sigma-Aldrich, Germany) was used (makes the live cells green), and the viable cells were observed under a fluorescence microscope (Nikon Eclipse Ti-e, Nikon Imaging, Czech Republic). To do this, first, 5×10^3 MC3T3-E1 cells/well were cultured with the complete culture medium for 24 h in a 96-well plate. The cells were then cultured with the scaffold extract media for 3 days. After that, the medium was removed, the cells were fixed with 4 % paraformaldehyde for 15 min at 4 °C, paraformaldehyde was discarded, and the cells were washed with PBS. Next, 0.1 % Triton was used for 15 min to permeabilize the cells, and the cells were subsequently exposed to 2 % bovine serum albumin (BSA) for 60 min. Finally, 1.3 μM phalloidin was added to the cells with 30 min incubation in dark. In addition, cell density and distribution were observed via the light microscopy at day 3.

2.9.7. Alkaline phosphatase activity

MC3T3-E1 cells (2×10^3 cells/well) were cultured in a 96-well plate for 24 h and then exposed to the scaffold medium extracts. The scaffold media was supplemented with osteogenic factors by 50 μg/mL ascorbic acid, and 10 mM β-glycerophosphate (Sigma-Aldrich, USA). An Alkaline Phosphatase (ALP) Colorimetric Assay kit (SensoLyte pNPP Alkaline Phosphatase Kit, Ana Spec Inc., USA) was used to assess the ALP activity after 7 and 14 days (SensoLyte pNPP Alkaline Phosphatase Assay Kit, Ana Spec Inc., USA). Osteoblasts lysate with Triton X-100 (100 μL/well) was incubated with the colorimetric ALP substrate (pNPP) at room temperature for 20 min. The ALP activity was measured at 405 nm, and the OD values were converted to concentrations using calf intestine for a calibration curve (the serial dilutions ranged from 100 to 0 ng/mL).

2.9.8. Alizarin red assay

Alizarin red staining (ARS staining), which is a marker of calcium deposition, was assessed after cell incubation for 10 days. This test was conducted twice; using scaffold extract media and by direct cell seeding on the scaffolds. In the first approach, 5×10^3 MC3T3-E1 cells/well were cultured in a 48-well plate placed in an incubator at 37 °C in CO_2 and 95 % humidity to form a cell monolayer (24 h). Afterward, the scaffold media with osteogenic agents containing 50 μg/mL ascorbic acid, and 10 mM β-glycerophosphate (Sigma-Aldrich, USA) were added. In the second approach, 5×10^3 cells/well were seeded directly on the scaffolds and osteogenic factors were added. After 10 days of incubation, cells in the presence of scaffold media and the seeded scaffolds were fixed with 4 % paraformaldehyde for 15 min at 4 °C, and the fixed samples were then washed with PBS and stained with 1 % (w/v) alizarin red for 40 min at room temperature in dark conditions. Finally, the samples were rinsed with PBS to remove unreacted alizarin red and observed under a loop microscope.

2.9.9. Immunocytochemistry

For immunocytochemistry (ICC), 1×10^4 MC3T3-E1 cells/well were seeded in 24-well plates and allowed to make a monolayer within 24 h for osteopontin (OPN) expression evaluation. Afterward, the cells in the presence of scaffold media supplemented with osteogenic factors (50 μg/mL ascorbic acid, and 10 mM β-glycerophosphate (Sigma-Aldrich, USA)) were incubated for 10 days. The adhered cells were fixed with a 4 % paraformaldehyde solution for 20 min, permeabilized with 0.3 % Triton X-100 for 30 min. The samples were washed with PBS and incubated with the primary antibody at 1:100 dilution. Then, the wells were washed with PBS to remove unbound antibody and the secondary antibody (1:150 dilution) was applied. After that, the plate was incubated with DAPI for nuclear labeling for 20 min. A fluorescence microscope (confocal Microscope—Olympus) was used to acquire the stained cells' images.

2.9.10. Cell adhesion study

Cell adhesion was assessed after 3 days of incubation. For cell adhesion, MC3T3-E1 (2×10^3 cells/well) were cultured directly onto the scaffolds at 37 °C in a humidified atmosphere containing 5 % CO_2 and 95 % humidity. Afterward, the scaffolds containing cells were first fixed with 4 % paraformaldehyde for 20 min and washed thrice with PBS. The dried samples were imaged by SEM after gold sputter-coating.

2.10. Statistical analysis

The presented data was performed in triplicate. Statistical analysis was performed using one-way or two-way analysis of variance (ANOVA). Moreover, GraphPad Prism version 9.00 and OriginPro 2018 were applied to draw the graphs. P-values <0.05 were used to determine statistically significant differences.

3. Results

3.1. Scaffolds characterization

Triangle-designed pore shapes were produced by 3D printing in accordance with the software design (Fig. 1Bi/ii). M-PCL with 54 ± 3 % porosity prepared as a 3D framework with interconnected architectures, and triangle pore pattern with a pore size of 709 ± 4 μm and strut thickness of 413 ± 7 μm (Fig. 1Biii). The surface modification did not significantly change the pore architectures, strut thickness, or dimensions but increased holes with nanoscale roughness on the fabricated struts. In addition, the EDS mapping analysis revealed the presence of the C and O elements in the PCL framework (Fig. 1Ci/ii/iii).

Next, the BG-containing TG sponges with three different concentrations of BG (10, 20, and 30 w/v%) were incorporated into the spaces within the M-PCL framework by a lyophilization method. FE-SEM images revealed that the TG-BG sponges were both successfully embedded between the M-PCL framework and deposited on the surface of the M-PCL. Furthermore, TG-BG sponges in the M-PCL framework exhibited a highly interconnected porous structure (Fig. 2Ai, Bi, Ci). The scaffolds exhibited >60 % porosity with pore size distribution in the range of

90–140 μm and the pore size decreased with the increasing amount of BG concentration. Pore size significantly increased at 10 % w/v, while pore size reduced at 30 % w/v, when BG content was increased. Although the introduction of BG to multi-compartment scaffolds increases biological activity, it (beyond 30 %) decreases the pore size to less than 100 μm, which is insufficient for cellular attachment and vascularization. Generally, pore diameter should be greater than 100 μm for cellular attachment and vascularization [18]. Thus, high BG content limits space and hinders ice crystal growth during freezing. Therefore, the size of entrapped ice blocks is reduced, and scaffolds with smaller pores are formed during sublimation. Additionally, as a result of the interaction between BG and TG, pores were reduced during freezing, resulting in smaller entrapped ice blocks, which formed scaffolds with smaller pores during subsequent sublimation. Furthermore, the presence of BG in the scaffolds was characterized by EDS mapping (Fig. 2). Si, Ca, and P were detected on the scaffolds that confirmed the incorporation of BG particles in M-PCL, and the distribution of BG was uniform in all three samples (Fig. 2ii/iii/iv/v). Three elements (Si, Ca, and P) were evaluated in scaffolds and the results are provided in Table 1. As expected, elements atomic percent increased by an increment of BG concentrations.

Table 1
Pore size, porosity and the elemental content of the scaffolds.

No	Pore size (μm)	Porosity (%)	Si content (At%)	Ca content (At%)	P Content (At%)
M-PCL	709 ± 4	54 ± 3	–	–	–
M-PCL/ TG-BG 10 %	133 ± 1	67 ± 0.5	2.76	2.39	0.33
M-PCL/ TG-BG 20 %	108 ± 8	77 ± 1	2.95	2.63	0.35
M-PCL/ TG-BG 30 %	91 ± 4	79 ± 0.5	2.98	2.70	0.39

3.2. FTIR and XRD analysis

FTIR analysis identifies the chemical composition of the organic/inorganic components in the scaffolds (Fig. 3A). The peak at 2925 cm^{-1} and 2895 cm^{-1} indicates the CH_2 groups and, 1741 cm^{-1} is related to the C═O groups of the M-PCL framework and TG component. The TG, as the organic component, detects its absorption peaks at 3444 cm^{-1} (stretching vibration of hydroxyl group), 1640 cm^{-1} (an asymmetrical stretch of the carboxylate group), and 1477 cm^{-1} (a symmetrical stretch of carboxylate group). As the inorganic component, the peaks at 874 cm^{-1}, 1090 cm^{-1}, and 3444 cm^{-1} are assigned for Si–O bending vibration, symmetric stretch vibration of Si–O, Si–O–Si stretch vibration, and OH group, respectively. Fig. 3B shows the XRD patterns of the M-PCL and the multi-compartment scaffolds. The two most intense peaks at approximately 21.44° and 23.78° are assigned to PCL; these peaks correspond to the (110) and (200). In multi-compartment scaffolds, the strong peaks at 2θ = 20–25°, are associated with the PCL crystal planes (110), and (200). Moreover, the TG and BG peaks resembled the PCL peaks, indicating that the TG and BG with amorphous structures do not have a crystal phase. In addition, the characteristic peaks of M-PCL were not significantly altered with increased BG, indicating that its crystallinity was not affected by incorporating BG. However, the intensity of the PCL peaks tends to decrease with the incorporation of TG and BG component.

3.3. In vitro bioactivity of scaffolds

Fig. 4 shows the FE-SEM images of scaffold surfaces after immersion in SBF. Precipitation was observed on the M-PCL and multi-compartment scaffold surfaces after 7 and 14 days of immersion. It was identified that the apatite layer was formed on the surface of multi-compartment scaffolds after immersing in SBF for 7 days, while in the case of M-PCL thin apatite layers were detected. After 14 days of

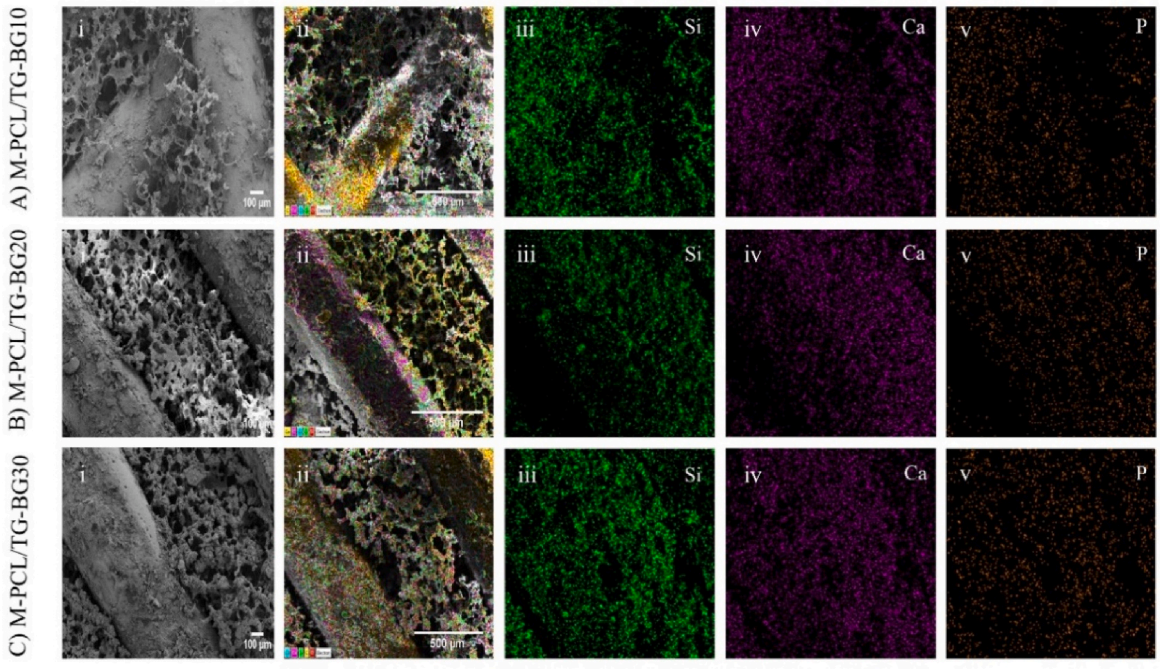

Fig. 2. A) The morphology of (i) M-PCL/TG-BG10 (scale bar: 100 μm), (ii) EDS mapping in the region of interest (scale bar: 500 μm), (iii-v) distribution of chemical composition respective for Si, Ca and P. B) The morphology of (i) M-PCL/TG-BG20 (scale bar: 100 μm), (ii) EDS mapping in the region of interest (scale bar: 500 μm), (iii-v) distribution of chemical composition respective for Si, Ca and P. C) The morphology of (i) M-PCL/TG-BG30 (scale bar: 100 μm), (ii) EDS mapping in the region of interest (scale bar: 500 μm), (iii-v) distribution of chemical composition respective for Si, Ca and P.

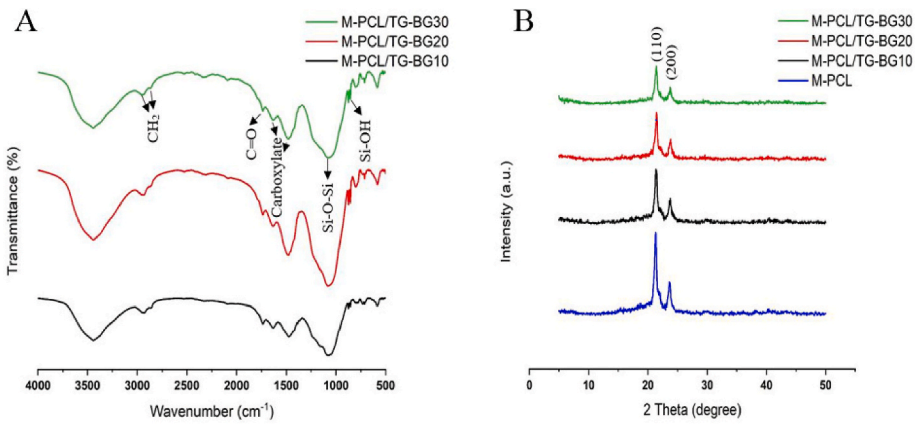

Fig. 3. A) The FTIR analysis of the scaffolds. B) The XRD analysis of the host and host-guest scaffolds.

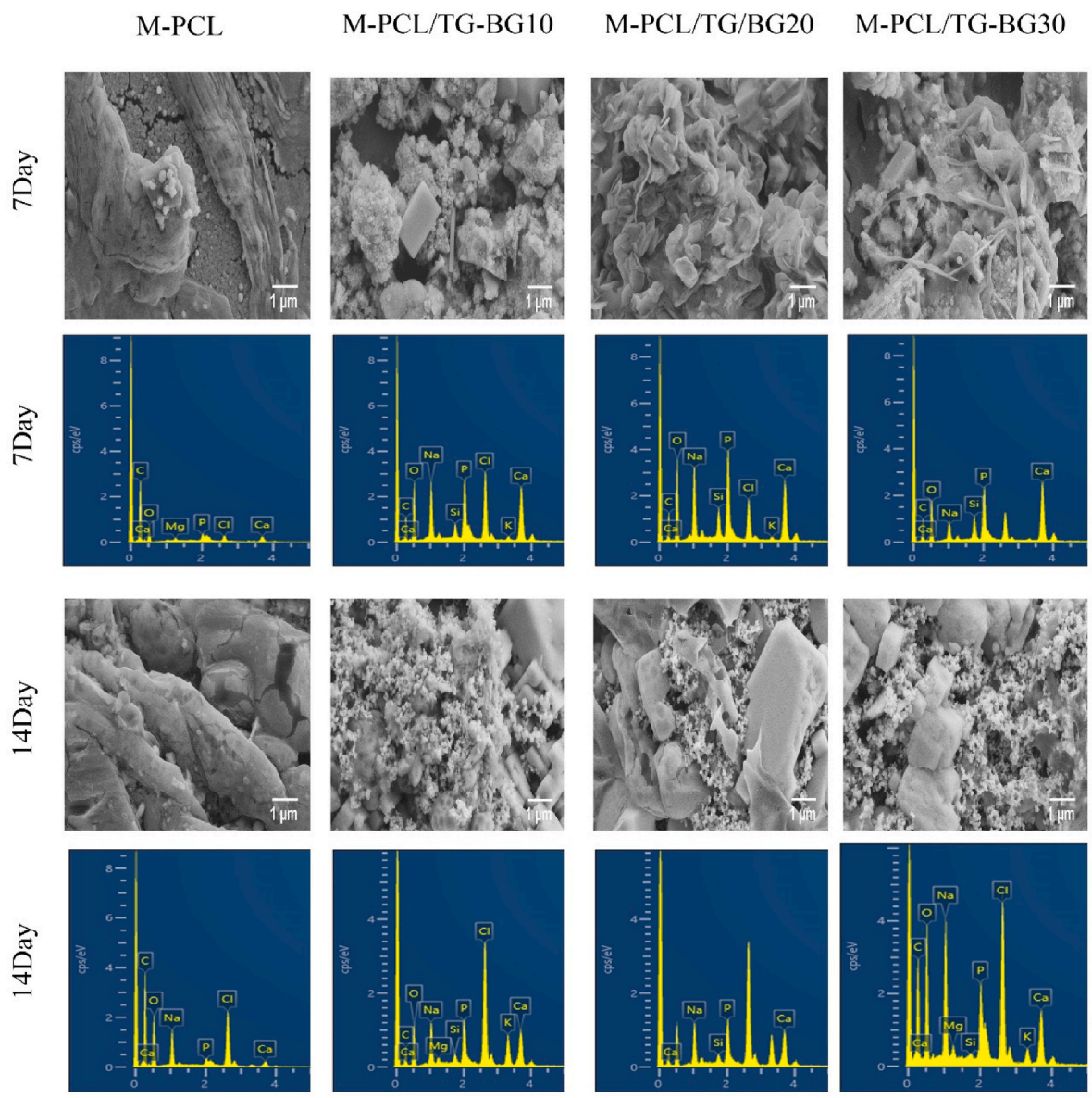

Fig. 4. FE-SEM micrographs of host and host-guest scaffolds after being immersed into SBF for 7 and 14 days (scale bar: 1 μm), and EDS spectra of scaffolds immersed into SBF for 7 and 14 days.

immersion, the precipitates formed a denser layer and covered the entire scaffold surface in comparison to M-PCL, and the globular shape hydroxyapatite (HAp) layers were relatively homogeneous. Despite this, visible cracks were observed on the M-PCL surfaces after 14 days of immersion in SBF, which was possibly due to the weak adhesion of the HAp layer. Moreover, the coating increased significantly with the increase in the soaking time, suggesting a continuous mineralization stage. EDS analysis on days 7 and 14 showed the Ca/P ratio of M-PCL and multi-compartment. The Ca/P ratio of the multi-compartment scaffolds is closer to the Ca/P ratio of the natural bone at 1.67 (Table 2). Therefore, the precipitates in multi-compartment scaffolds were calcium- and phosphorus-rich phases. Furthermore, from the EDS analysis, it is evident that the Si on the surface reduced considerably. It is believed that the low detection of Si is due to precipitated apatite on the multi-compartment scaffolds.

Ion release from multi-compartment scaffolds to the SBF during incubation is shown in Fig. 5. In multi-compartment scaffolds, Ca and P concentrations decreased, confirming apatite layer formation on their surfaces (Fig. 5B and C). In addition, the release rate of Si to SBF from scaffolds with higher BG content significantly increased, corresponding to the dissolution of BG from the scaffolds (Fig. 5A). Initial ion exchange was accomplished by scaffold immersion in the solution during the early days. During the process, Ca^{2+} ions in the environment were replaced with H_3O^+ ions. Additionally, the solution's ion exchange was significantly altered by incorporating the phosphate ions to replace the hydroxyls. Thus, silanols were formed from the attack on the silicate glass network caused by an increased hydroxyl concentration in the solution [19]. The pH of the immersion medium was measured at all time intervals. The pH of the immersion medium of M-PCL remained relatively constant throughout the 2 weeks (Fig. 5D). The pH level related to the media of the multi-compartment scaffolds was between pH 7.71 to 7.83. After 24 h of immersion, the pH of the media increased from pH 7.4 to pH of about 7.71–7.74. In addition, scaffolds with higher BG contents showed significant pH increases due to the increasing replacement of Ca^{2+} ions with H_3O^+ ions. This process led to the nucleation and crystallization of the apatite. The pH of media associated with the multi-compartment scaffolds increased up to 6 days. After 6 days of soaking, the pH decreased, which might be the result of the formation of a bioactive layer on the surface of the scaffolds and then the pH was constant. After immersion of scaffolds in SBF, characteristic absorption bands of apatite were indicated such as the presence of phosphate groups at about 584, 628, and 1049 cm^{-1} (Fig. 5E). Fig. 5F shows the XRD patterns of the mineralized scaffolds. XRD analysis confirmed that the scaffolds exhibited apatite deposition within 7 and 14 days of immersion in SBF. The most intense HAp crystal peak corresponds to the (2 1 1) reflection at $2\theta = 31.52°–31.76°$ and the peak at $2\theta = 45.56°–45.68°$ is related to the (2 2 2) reflection. The low intensity of peaks is due to the low crystalline or nanosized range of crystals of newly formed HAp.

Table 2
The Ca/P ratio of the scaffolds after immersion into SBF and mechanical properties of scaffolds.

No	Ca/P ratio (7d)	Ca/P ratio (14d)	Compression strength (MPa)	Compression modulus (MPa)
M-PCL	1.01 ± 0.2	1.23 ± 0.01	6.58 ± 0.3	9.55 ± 0.3
M-PCL/TG-BG 10 %	1.44 ± 0.2	1.64 ± 0.4	10.38 ± 0.4	14.15 ± 0.3
M-PCL/TG-BG 20 %	1.51 ± 0.7	1.83 ± 0.3	17.62 ± 0.4	17.49 ± 0.4
M-PCL/TG-BG 30 %	1.64 ± 0.5	1.88 ± 0.3	23.11 ± 0.2	23.48 ± 0.4

3.4. Scaffold degradation

Fig. 6A shows the weight loss of the scaffolds at different time intervals (1, 3, 7, 14, 21, and 28 days) in SBF solution (pH = 7.4) at 37 °C. According to the results, scaffold degradability increased with the BG content. It was demonstrated that TG-BG increased the degradability of scaffolds due to hydrolytic degradation behavior along with the ions release (e.g., Si and Ca). BG typically has a high tendency to initiate the rapid exchange of ions with the surrounding environment fluid. Thus, scaffolds with higher content of BG expectedly released higher amounts of dissolved ions into the environment. Therefore, the 30 % BG scaffold demonstrated the highest degradation at each time interval. Moreover, as the incubation time increased, the rate of degradation increased so that after 7 days, multi-compartment scaffolds demonstrated a weight loss percentage of around 21–50 %. Functional groups of TGs (COOH, OH) can electrostatically react with Ca of BG; in addition, due to the abundant carboxyl groups on multi-branched heterogeneous anionic TG, $CaCl_2$ reacts with the COOH moieties to initiate the crosslinking process. In this regard, while the TG material was displaying its degradation features, the addition of BG could noticeably affect the degradation behavior of the multi-compartment scaffolds. In contrast, the PCL frameworks were degraded very slowly; the weight loss was approximately constant after 21 days due to the unaffected PCL structure.

3.5. Mechanical properties of scaffolds

The mechanical properties of the scaffolds were measured to evaluate the effect of the TG-BG on the mechanical properties of the framework (Fig. 6B and C). The results suggest that incorporating TG-BG increased the compressive modulus of the M-PCL constructs. As it is expected, the compressive modulus of the multi-compartment scaffolds was significantly different ($p < 0.0001$). Compressive strength significantly increased by the increase of BG from 10 % to 30 %, both falling into the stiffness range of native cancellous bone and possibly providing mechanical support during the formation of new bone (Table 2).

3.6. In vitro biocompatibility evaluation

MC3T3-E1 cell viability cultured in the presence of scaffold extracts was evaluated using LDH assay after 1, 3, and 7 days (Fig. 7A). The ANOVA results showed that the scaffolds, time, and scaffolds*time ($P = 0.000$) play a significant role in cell viability. Based on the high cell viability of the scaffolds, any cytotoxic effect was rejected. The least viability was associated with M-PCL. The cell viability of M-PCL/TG-BG in the different ratios was significantly higher than M-PCL. Therefore, the scaffolds are considered non-toxic.

Fig. 7B represents the proliferation of the cells using MTT assay. Two-way ANOVA was employed to evaluate the proliferation of MC3T3-E1 cells exposed to the medium extracts of the fabricated scaffolds. Significant factors ($P = 0.000$) included scaffold, time, and scaffold*times, suggesting that the composition of scaffolds influenced cell proliferation. As shown in Fig. 7B > 70 % of MC3T3-E1 cell proliferation in the presence of M-PCL scaffold extract was observed on 1, 3, and 7 days. Unlike M-PCL, the cells exhibited different proliferation profiles by different ratios of M-PCL/TG-BG. It was observed that the cell proliferation increased on day 3 and significantly decreased on day 7. Surprisingly, at the early stage, the proliferation percentages for the scaffolds were high, and these percentages decreased over time, indicating that the materials had a greater effect on cellular metabolism at that time. This might be due to the fact that the cells in these groups underwent differentiation process as the LDH analysis rejected any cytotoxic effect caused by the scaffolds.

The osteocalcin levels were observed on day 7 in Fig. 7C. The level of osteocalcin in the M-PCL/TG-BG30 was significantly different from other groups. After 7-day induction, M-PCL/TG-BG30 induced much higher osteocalcin levels than other groups, indicating that this scaffold

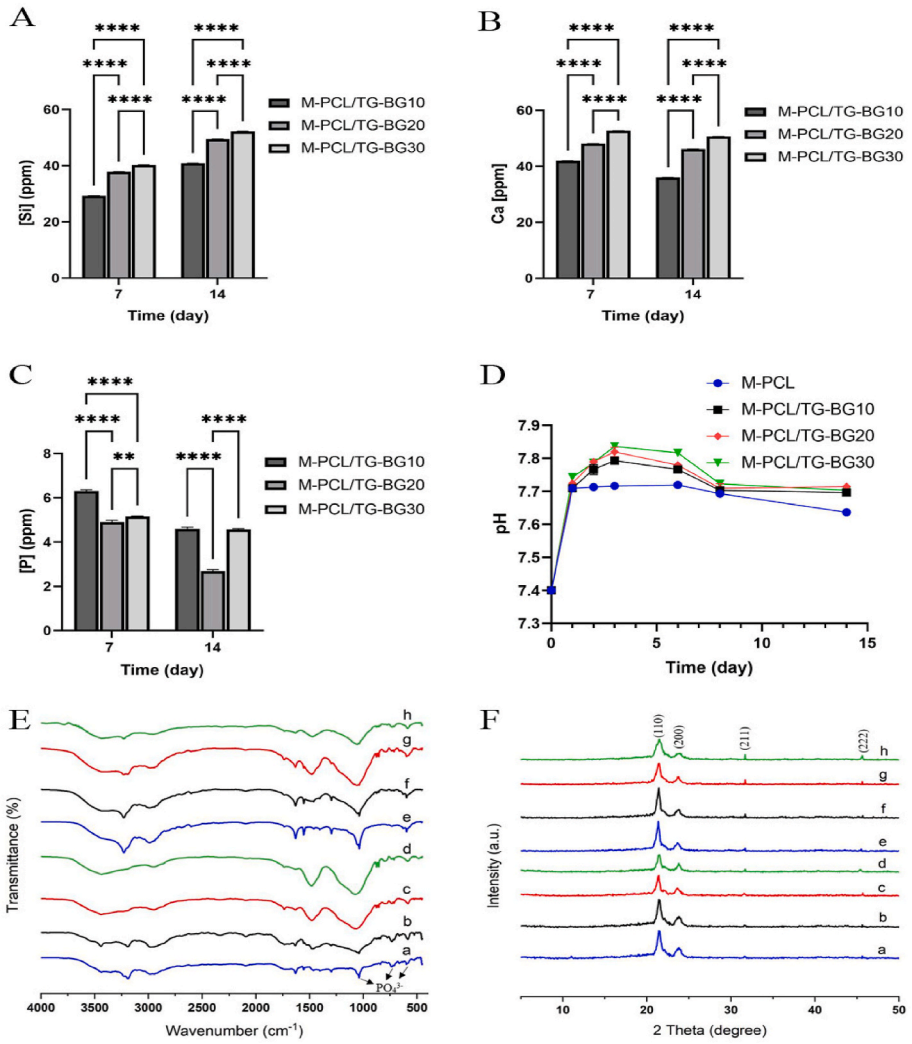

Fig. 5. A-C) Si, Ca, and P ion concentration of host-guest scaffolds for 7 and 14 days (**, $p < 0.01$; ****, $p < 0.0001$). D) pH value of media with immersed host and host-guest scaffolds. E) The FTIR analysis of the host and host-guest scaffolds after immersion in SBF, (a–d) FTIR analysis respective for M-PCL, M-PCL/TG-BG10, M-PCL/TG-BG20, M-PCL/TG-BG30 in day 7, (e–h) FTIR analysis respective for M-PCL, M-PCL/TG-BG10, M-PCL/TG-BG20, M-PCL/TG-BG30 in day 14. F) The XRD analysis of the host and host-guest scaffolds after immersion in SBF, (a–d) XRD analysis respective for M-PCL, M-PCL/TG-BG10, M-PCL/TG-BG20, M-PCL/TG-BG30 in day 7, (e–h) XRD analysis respective for M-PCL, M-PCL/TG-BG10, M-PCL/TG-BG20, M-PCL/TG-BG30 in day 14.

could significantly enhance the osteogenic differentiation of MC3T3-E1 cells.

To visualize the cell distribution in the presence of the scaffolds, the dense collection of cells was imaged (Fig. 7D and E). The cell proliferation regulated by M-PCL/TG-BG was comparable to that of the control and M-PCL group. Individual cells could be observed in some parts of the control and M-PCL wells, while cells covered the majority of the culture surface in the presence of M-PCL/TG-BG extracts which showed confluent growth. In addition, a thick and spread-out distribution of cells in the presence of the multicompartment scaffold was found, whereas, the void spaces were observed, on the control and M-PCL scaffold groups. As expected, the cell distribution depended on the scaffold biomaterial.

3.7. Alkaline phosphatase activity

ALP assay was used to evaluate the osteogenic potential of the pre-osteoblasts MC3T3-E1 cells (the osteogenic function) exposed to the scaffold extracts at two-time intervals. ALP activity of different scaffolds was similar, while the ALP activity increased by the culture time. The ALP concentration increased at a low rate from day 7 to day 14 as shown in Fig. 8A. Two-way ANOVA also revealed that scaffold was not a significant factor ($P = 0.59$), but time ($P = 0.000$) was.

3.8. Matrix mineralization

For quantification of mineralization and calcium deposit, MC3T3-E1 cells cultured in the scaffold medium extracts or seeded on the scaffolds with osteogenic factors were stained using a calcium-staining Alizarin Red kit after 10 days. Fig. 9A shows the Alizarin Red staining of the cells exposed to different media, and direct cell-seeded scaffolds after osteogenic induction at day 10. Fig. 9A also compares the cell-seeded scaffolds to the scaffolds without cell-seeding as the M-PCL/TG-BG scaffolds already had Ca content. The percentages of the red-stained area in the presence of scaffold media were quantified (Fig. 8B). As observed, red nodules were established on all scaffold surfaces. The highest mineralization was found in the presence of M-PCL/TG-BG with different ratios, and the mineralized area was expanded by higher BG content. On the 10th day of differentiation, the M-PCL/TG-BG 20 and 30 scaffolds was stained a more robust red color compared to the other groups, and this means that the calcium deposition was highest compared to other groups. As shown in Fig. 9A, no positive red stains were found on M-PCL

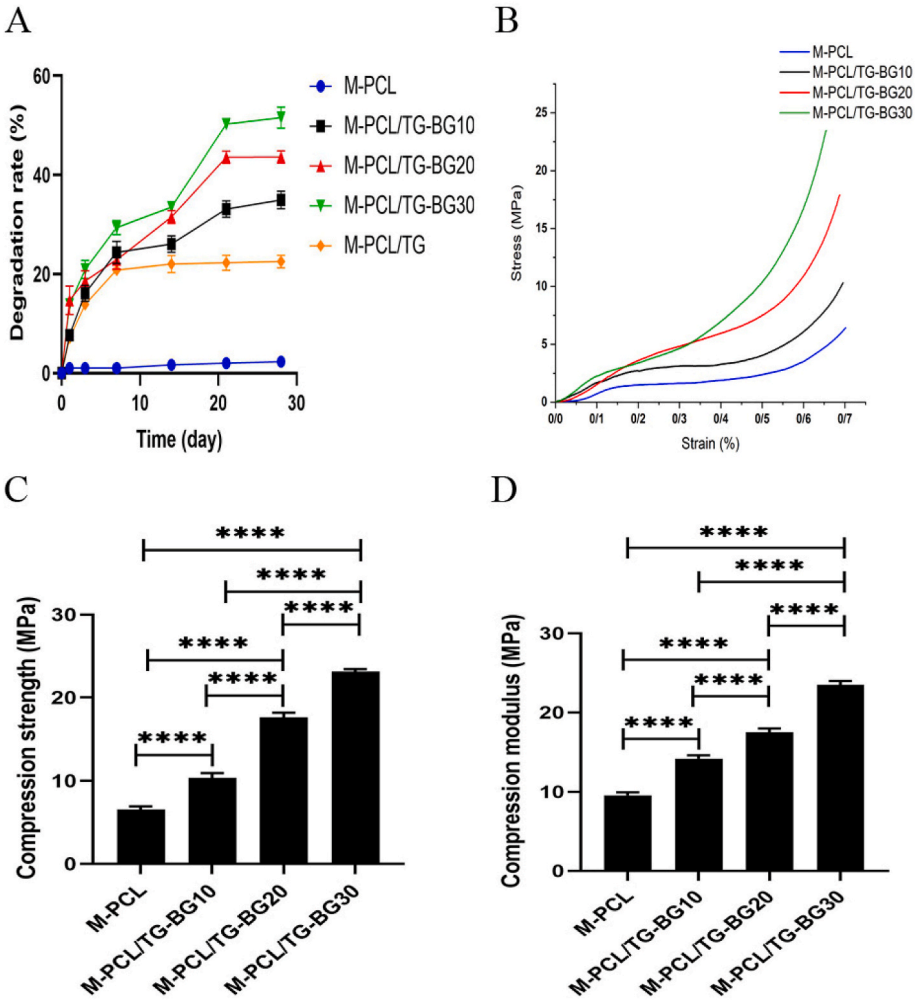

Fig. 6. A) Biodegradation rate of the host and host-guest scaffolds. B) Stress–strain curves of the host and host-guest scaffolds. C) Compression strength of the host and host-guest scaffolds (****, $p < 0.0001$). D) Compression modulus of the host and host-guest scaffolds (****, $p < 0.0001$).

before cell-seeding. In contrast, multi-compartment scaffolds confirmed the presence of calcium. However, a significant difference was between the formation of mineralized nodules of the cell-seeded scaffolds and the control groups.

3.9. Immunocytochemistry (ICC)

Immunocytochemistry assay was performed on the osteoblast cells differentiated from MC3T3-E1 cells in osteogenic media after 10 days by analyzing the osteopontin level (Fig. 9B). The expression of osteopontin protein of the cells exposed to PCL/TG-BG30 extracts significantly increased compared to other groups on day 10. Thus, the increase in the BG content accelerated the osteogenic induction and led to higher level of bone-specific marker expression as early as 10 days. In addition, PCL/TG-BG20 and PCL/TG-BG10 showed higher expression of osteogenic markers compared to M-PCL group.

3.10. Adhesion of cells to the scaffold surface

SEM images inferred the capability of the scaffolds on MC3T3-E1 cell morphology and attachment. It is clear from Fig. 9C that the adhered cells on different scaffolds exhibited different morphologies. The cells were quite a spheroid shape on M-PCL and the number of cells was low. Furthermore, the cells increased on the surfaces of M-PCL/TG-BG with different ratios, particularly with an increase of BG content, the cell attachment increased. As the BG content increased, the surface of the scaffolds was covered with the proliferated cells, which indicated that the scaffolds provided a suitable micro-environment for the growth of MC3T3-E1 cells. In this way, a layer of cells covered almost entirely the substrate in M-PCL/TG-BG, indicating a better ability for cell adhesion than in M-PCL.

4. Discussion

As an ideal bone graft substitute for clinical use, concise control on the porous scaffold's architectures can facilitate cells/tissues ingrowth and delivery of nutrients. In this context, the scaffold architectures such as pore size, pore morphology, porosity, and pore interconnectivity could be adjusted by 3D printing techniques [20]. Therefore, in this study, we further proposed the TG-BG matrix as a guest component that integrated with 3D macroporous PCL framework. In comparison to guest components, the framework offers mechanical support, and biodegradability over an extended period of time. Unfortunately, poor biological performance of PCL scaffolds leads to lack of cell adhesion, in vivo fibrous encapsulation, and are incapable of osseointegration or bone tissue repair, ultimately leading to the failure of bone defect treatment [21]. The PCL scaffold activity was found to be enhanced by alkaline treatment with increases in nanoscale surface roughness and wettability due to the hydrophilic surface groups such as carboxyl and hydroxyl groups [22]. Based on the previous study, 3D models with different pore sizes and pore shapes were designed using CAD software and deposited layer-by-layer following a specific laydown pattern by 3D printing.

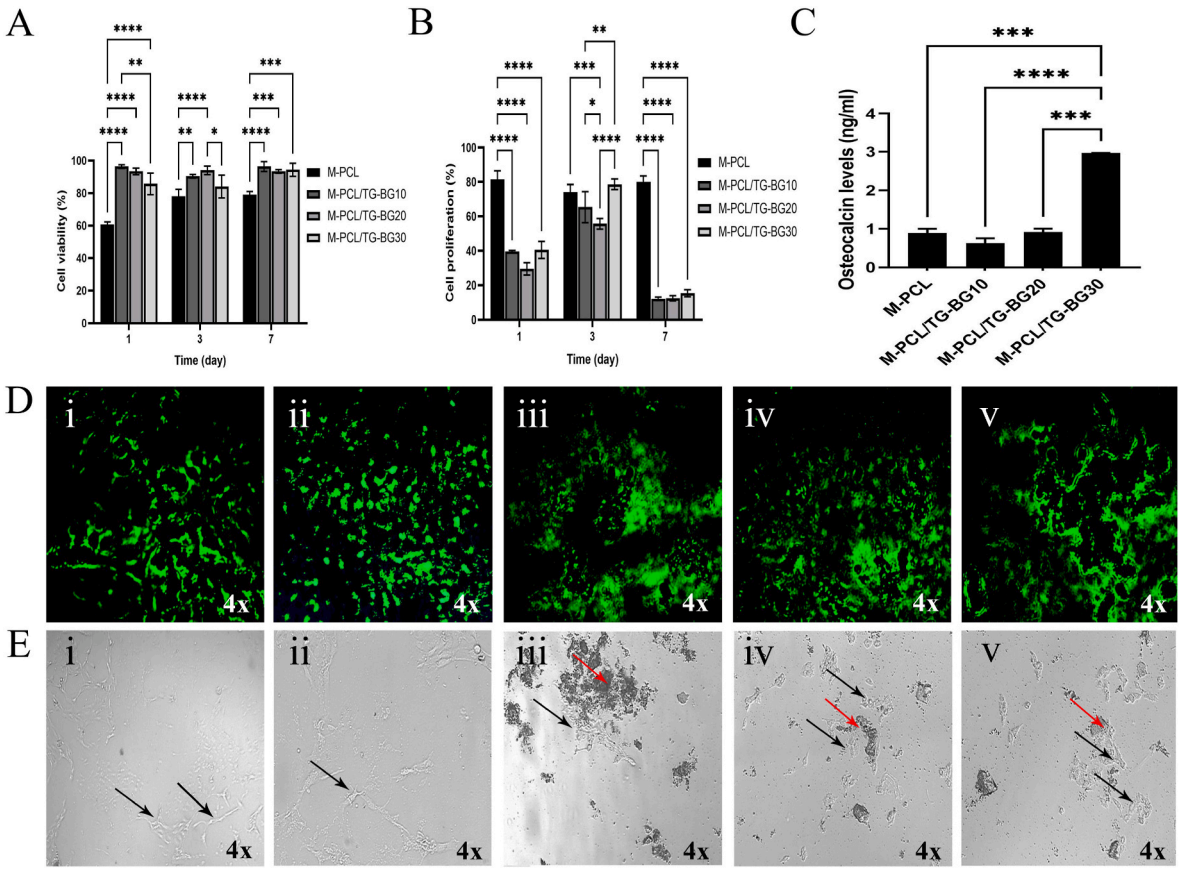

Fig. 7. A) Cell viability of the host and host-guest scaffolds on 1, 3 and 7 days. B) Cell proliferation of the host and host-guest scaffolds on 1, 3 and 7 days. C) Osteocalcin levels of the host and host-guest scaffolds on day 7. D) Cell density and distribution at day 3 (i: cell, ii: M-PCL, iii: M-PCL/TG-BG10, iv, M-PCL/TG-BG20, v: M-PCL/TG-BG30; green color: live cells; images are shown at 4× magnification). (*, $p < 0.05$; **, $p < 0.01$; ***, $p < 0.001$; ****, $p < 0.0001$). E) The light microscopy images of cell density and distribution at day 3 (i: cell, ii: M-PCL, iii: M-PCL/TG-BG10, iv, M-PCL/TG-BG20, v: M-PCL/TG-BG30; black arrows: cells, red arrows: BG; images are shown at 4x magnification). (For interpretation of the references to colour in this figure legend, the reader is referred to the Web version of this article.)

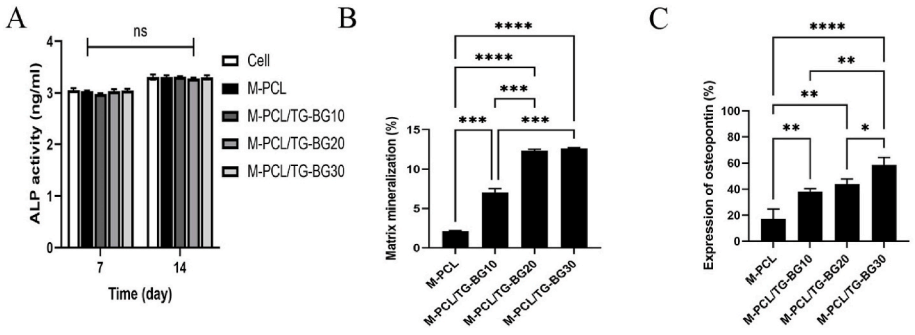

Fig. 8. A) ALP activity of the host and host-guest scaffolds on 7 and 14 days. B) Matrix mineralization of the host and host-guest scaffolds on day 10. C) Osteopontin expression of the host and host-guest scaffolds on day 10. (ns, no significant; *, $p < 0.05$; **, $p < 0.01$; ***, $p < 0.001$; ****, $p < 0.0001$).

Among the sixteen designs, T7001 with a pore size of 700 μm, pore shape of the triangle, and surface treatment with 1 M NaOH had proper surface roughness, porosity, interconnectivity, mechanical properties like those of cancellous bone, bioactivity close to hydroxyapatite, cell viability, and biomineralization [12]. Specifically, in our study, the macroporous PCL framework was meticulously fabricated using the 3D printing technique with a pore size of 700 μm and modified with NaOH solution in 1 M concentration. Macropores are designed to provide more space for bone tissue ingrowth. Moreover, the etching of the PCL surface produces a hydrophilic rough surface, which would permit the TG-BG to be immobilized onto the surface of the scaffold. In addition, the 0°-60°–120° lay-down pattern was selected to entrap the TG-BG between the layers of the scaffolds. Afterward, the TG-BG was incorporated into the M-PCL framework to provide the ECM for bone regeneration. This structure not only increased cell entrapment and differentiation but also provided the matrix for biomineralization and tissue growth [23].

It was found that the apatite mineralization of scaffolds increased with increasing BG content, indicating that incorporating BG into the scaffolds might boost apatite mineralization abilities. Two weeks after immersion of M-PCL framework containing TG-BG matrix, precipitates formed on the surfaces of the scaffolds implied an improved in vitro bioactivity of the scaffold. Especially, the M-PCL/TG-BG20 and M-PCL/

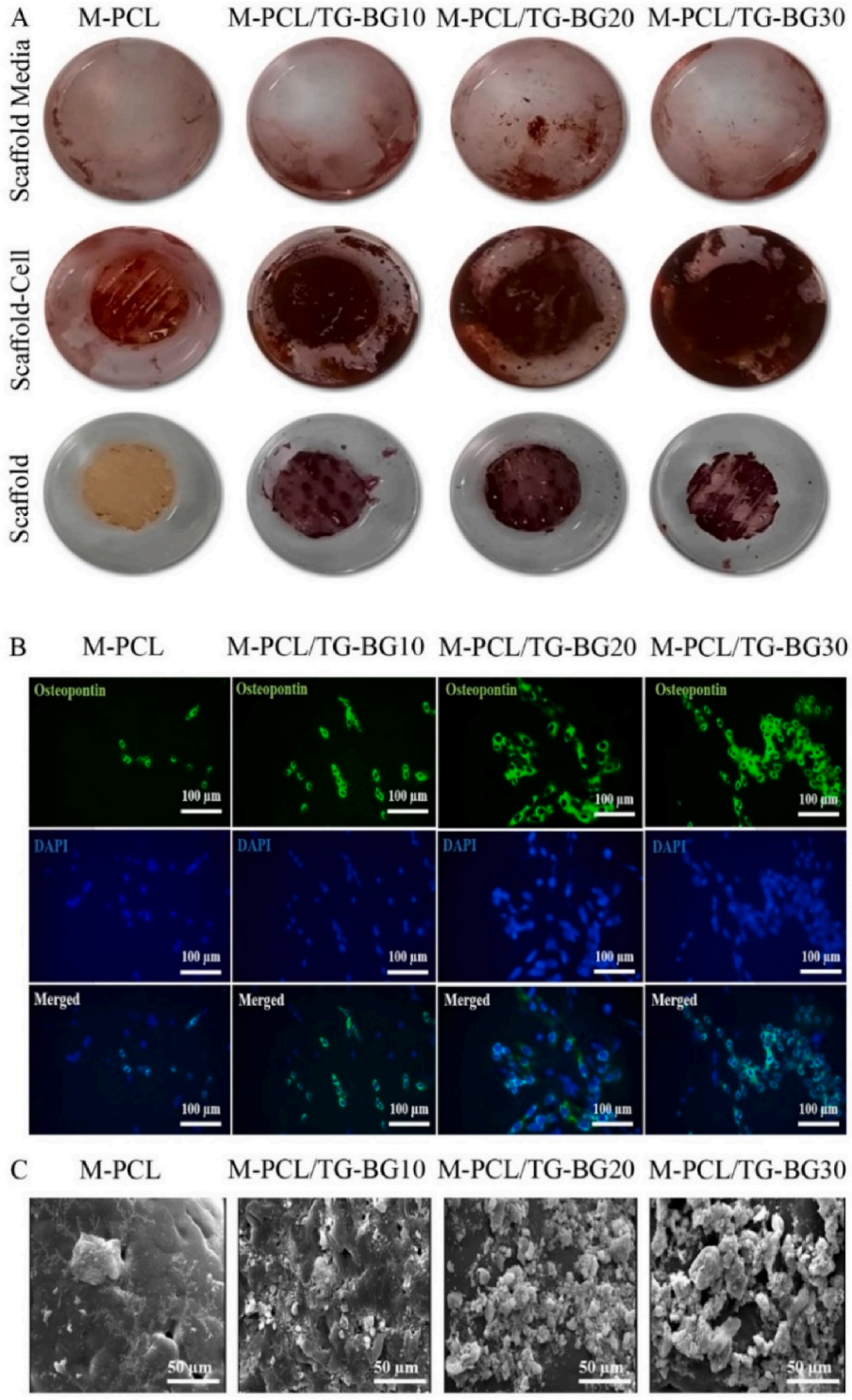

Fig. 9. A) ARS staining showing calcium deposition by scaffold media, cell-seeded scaffolds and scaffolds as control. B) Immunofluorescence staining of osteopontin expression in MC3T3 E1 cells (OPN: green, nuclei: blue; scale bar: 100 μm). C) Cell adhesion on host and host-guest scaffolds (scale bar: 50 μm). (For interpretation of the references to colour in this figure legend, the reader is referred to the Web version of this article.)

TG-BG30 scaffolds exhibited the highest apatite mineralization close to the native bone. The HAp deposits gradually and covered the matrix, which mimics the composition of bone minerals and encourages osteointegration and subsequent bone tissue formation. According to the SEM images, the calcium phosphate formation area on the surface of the M-PCL framework was not completely homogeneous, but the M-PCL/TG-BG scaffolds showed a relatively homogeneous coating. We found that the negatively charged carboxylate groups on the surface of the TG and the chemical compositions of bioactive glass could facilitate in vitro biomineralization and improve the nucleation of the HAp [24]. The ion release profiles of Si, Ca, and P from the multi-compartment scaffolds in the media, and the EDS analysis of the scaffolds confirmed that the precipitates formation on M-PCL framework and multi-compartment scaffolds were different. Typically, during the dissolution of BG,

released ions such as Ca^{2+} are exchanged with H^+ and H_3O^+ of the surrounding media, and then a silica-rich layer is created where heterogeneous nucleation and crystallization of a biologically reactive apatite layer can occur [25]. Furthermore, the pronounced pH rise in the immersion media of multi-compartment scaffolds is caused by some released ions of BG. Initially, the pH increases to aid the formation of apatite, then reduces over time due to the gradual formation of apatite layer [26]. In contrast to other groups, M-PCL/TG-BG30 displayed a higher pH, possibly indicative of a higher BG concentration. Moreover, M-PCL framework showed no significant change in pH value compared with the initial value.

Bone tissue engineering scaffolds need to degrade at a rate that matches the new bone formation by in-vivo implantation [27]. In this study, the results displayed that the incorporation of TG-BG matrix into the M-PCL framework could expand their degradability, in which M-PCL/TG-BG30 scaffold possessed the fastest degradation rate. Moreover, the release of Si and Ca ions into the micro-environment due to the dissolution of BG would lead to the degradation of scaffolds. The degradation of M-PCL/TG-BG with different ratios in the media increased with time while no noticeable change for M-PCL framework was observed [28,29]. PCL framework had first-rate degradation, whereas, the TG-BG matrix showed a second degradation rate. First-rate biodegradation is slower than the second-rate biodegradation. The framework with its slow degradation could replace with new bone tissue over time and provides structural support over a longer time without the need for additional surgery. Moreover, the rapid degradation of TG-BG in multi-compartment scaffolds enables the release of ions for new tissue formation, in contrast, the remaining M-PCL provides additional mechanical support for neo-tissue. In the fabrication of scaffolds, porous structures providing superior biological performance should be carefully balanced with a dense scaffold that provides better mechanical performance [30]. To improve the shortcomings of the TG-BG matrix, we used PCL as a framework for structural support. We reported here that the mechanical properties of these scaffolds are close to the trabecular bone. Despite M-PCL/TG-BG scaffolds showing compressive strengths close to the cancellous bone (2–12 MPa), the compressive Young's moduli of scaffolds are not yet similar to the native bone (0.05–0.5 GPa) [31]. Therefore, multi-compartment scaffolds could assist bone regeneration at low load-bearing sites.

Ideal scaffolds for bone tissue regeneration should provide an environment for cell proliferation, which imitates natural bone ECM and enhances the formation of new bone [32]. The results of the present study confirmed that the MC3T3-E1 cell viability on the scaffolds was significantly enhanced in the presence of TG-BG matrix, and scaffolds displayed the highest ability to promote cell viability compared to M-PCL framework [24]. The nontoxic effect of the multi-compartment scaffolds was verified by the LDH release measurement from the cells. With regard to cell proliferation, the reduction of metabolic activity after 3 days on the multi-compartment scaffolds compared with the M-PCL, might be due to the increased differentiation of pre-osteoblast MC3T3-E1 cells toward osteoblastic cells. This may be due to the fact that pre-osteoblast cells have the ability to change their form and function in response to their environment. During the osteogenic differentiation phase, pre-osteoblast cells proliferate slowly. Consequently, the MC3T3-E1 cells in all three groups of the scaffolds showed a lower metabolic activity with the prolonged culture time due to differentiation. Ruijtenberg and Heuvel comprehensively explained the mechanism for an inverse relationship between cell proliferation and differentiation. Furthermore, it has been indicated that the metabolic shifts (between aerobic glycolysis and oxidative phosphorylation) during cell differentiation are possibly due to the specific cell identities obtained [33]. This change affects many processes including biosynthesis, the state of intracellular redox, epigenetic status, and the level of reactive oxygen species (ROS) which influence adenosine triphosphate (ATP) synthesis and subsequently impact cell behavior such as proliferation [34–36]. The cell distribution of MC3T3-E1 was observed by fluorescence microscope on day 3. Many more live cells were distributed (higher cell distribution) in the M-PCL/TG-BG groups, especially those with 20 % and 30 % BG, compared to those in M-PCL. Therefore, all the scaffolds exhibited good cytocompatibility. As a result, we believe that the osteoblast-like cells possess the ability to proliferate as a result of continuously released ions from the scaffolds [37].

ALP activity, an early marker of the osteoblast differentiation, is generally regarded as an indicator of osteogenesis in vivo [38]. As a result of analyzing ALP activity, it was found that the scaffolds induced osteogenic differentiation [39]. Moreover, the osteopontin and osteocalcin expression measurements were used to quantify and compare cell differentiation between the scaffolds. Typically, mature osteoblasts secrete OCN and represent the terminal differentiation of osteoblasts [40]. Remarkably, the OCN upregulation for M-PCL/TG-BG (especially 30) in non-osteogenic media revealed that osteoblast differentiation could better promote in the presence of BG compared to M-PCL. The osteo-supplemented media can enhance osteoblast differentiation. As an early marker of pre-osteoblast proliferation in vitro, OPN is expressed in the bone marrow during osteoblast progenitor differentiation [41]. A remarkable consequence of this study is that the M-PCL framework, combined with TG-BG matrix, could induce cytoskeleton development, among other cellular activities. The cytoskeleton and nuclear staining results demonstrated the significant difference in the number of MC3T3-E1 cells on the different scaffolds. However, cells in the presence of higher BG content revealed a superior spread with a better cytoskeleton than on M-PCL. The presence of BG dissolution ions (e.g., Si, Ca, etc.) in the culture media can subsequently influence osteoblast proliferation and differentiation. Therefore, the improvements in OCN and OPN of MC3T3-E1 cells were related to the release of BG ions from the scaffolds [31,42]. As well, the apatite formation on the scaffolds might stimulate cell responses. As a late-stage marker of osteogenic differentiation, mineral deposition is a useful marker to confirm that MC3T3-E1 cells have entered the mineralization phase to deposit mineralized ECM [43]. In the ARS staining images of the scaffolds, the red nodule defines the calcium mineral deposition area and with the increased BG content, a denser nodule was observed in all scaffolds. Especially, for the M-PCL/TG-BG30 and M-PCL/TG-BG20 scaffolds, the color density increased compared to the M-PCL/TG-BG10 and M-PCL framework, meaning increased calcium mineralization. This result can be attributed to the combined effects of the BG and TG promoting osteogenic differentiation of the cells. Additionally, the results of the cell adhesion indicated that the cell growth and the amounts of the cells in the M-PCL/TG-BG (20 and 30) scaffold were more than in M-PCL/TG-BG10 and M-PCL framework. This indicates that the M-PCL/TG-BG (20 and 30) scaffolds not only promoted cells proliferation but also stimulated cells migration into the scaffolds [44]. The limited adhesion of cells to the M-PCL framework can be attributed to PCL's hydrophobicity and its porous structure that does not support cell adhesion [45]. A common feature of scaffolds produced by 3D printing are interconnected open pores. A cell suspension can easily pass through these pores, which reduces seeding efficiency [46]. As a consequence of the insertion of the TG-BG matrix between the PCL framework, the cell suspension is likely to flow through the pores more slowly, thus increasing the surface area and cell adhesion. On day 3, the scaffolds were almost entirely covered by a layer of the cells. The attachment and expansion of the cells to the M-PCL/TG-BG (20 and 30) were higher compared to the other groups.

In summary, the results indicated that the HAp formation, mechanical properties, cell viability, degradability, and osteogenesis of the M-PCL/TG-BG scaffolds (especially 30) were attributed to the bioperformances of the TG and BG in the scaffolds, and the addition of M-PCL as a framework might be an effective component to improve the physical support. The shape, dimensions, and thickness of the framework can be matched with the size of the patient's bone damage. Besides, the TG-BG matrix that homogeneously filled the voids among the PCL framework can also assist as a microporous structure to induce the space for new bone formation and guide the bone regeneration.

5. Conclusion

To achieve optimal bone tissue ingrowth, an exceptional bone graft substitute must strike a delicate balance between mechanical functionality and biological performance. In the present study, we successfully integrated the TG-BG matrix as a guest component into a 3D-printed M-PCL framework, thus imparting favorable mechanical and biological properties to the scaffold. Firstly, our findings demonstrated that the inclusion of TG-BG significantly enhanced the in vitro bioactivity and degradability of the framework. This augmentation of bioactivity promoted cellular interactions and facilitated the scaffold's integration with the surrounding tissue. Additionally, the results revealed that the multi-compartment scaffolds exhibited high mechanical strength when compared to the framework alone, ensuring the required structural support for bone regeneration. Moreover, the presence of the TG-BG matrix within the framework demonstrated remarkable effects on the viability, proliferation, and differentiation of MC3T3-E1 cells, a model cell line used to study bone tissue. The TG-BG incorporation led to increased osteocalcin activity, upregulated osteopontin expression, and enhanced mineralization, indicating the induction of osteogenic properties and the potential for robust bone formation. By combining the benefits of TG-BG matrix with the 3D-printed PCL framework, our study highlights the exceptional potential of these multi-compartment scaffolds as effective bone graft substitutes for bone tissue regeneration. The results underscore their viability as a promising in vitro bone model, which can serve as a valuable tool for further preclinical investigations and facilitate the translation of these findings into clinical applications. The significant advancements made in developing these multi-compartment scaffolds hold great promise for improving the understanding of bone substitutes and accelerating their clinical translation. This research contributes to the ongoing efforts in the field of bone tissue engineering, providing a steppingstone towards the development of more effective bone graft substitutes for clinical applications.

Credit author statement

Mahsa Janmohammadi, Conceptualization, Methodology, Formal analysis, Investigation, Writing - Original Draft. Mohammad Sadegh Nourbakhsh, Supervision, Conceptualization, Methodology, Writing - Review & Editing, Marjan Bahraminasab, Supervision, Conceptualization, Methodology, Writing - Review & Editing, Author 4: Lobat Tayebi, Conceptualization, Writing - Review & Editing.

Declaration of competing interest

The authors declare that they have no known competing financial interests or personal relationships that could have appeared to influence the work reported in this paper.

Data availability

Data will be made available on request.

Acknowledgment

L.T. acknowledges the partial support from National Institute of Dental and Craniofacial Research of the National Institutes of Health under award numbers R56DE029191 and R15DE027533.

References

[1] L. Vidal, C. Kampleitner, M.Á. Brennan, A. Hoornaert, P. Layrolle, Reconstruction of large skeletal defects: current clinical therapeutic strategies and future directions using 3D printing, Front. Bioeng. Biotechnol. 8 (2020) 61.
[2] P.L. Rodham, V.P. Giannoudis, N.K. Kanakaris, P.V. Giannoudis, Biological aspects to enhance fracture healing, EFORT Open Rev. 8 (5) (2023) 264–282.
[3] M. Bahraminasab, M. Janmohammadi, S. Arab, A. Talebi, V.T. Nooshabadi, P. Koohsarian, M.S. Nourbakhsh, Bone scaffolds: an incorporation of biomaterials, cells, and biofactors, ACS Biomater. Sci. Eng. 7 (12) (2021) 5397–5431.
[4] M.N. Collins, G. Ren, K. Young, S. Pina, R.L. Reis, J.M. Oliveira, Scaffold fabrication technologies and structure/function properties in bone tissue engineering, Adv. Funct. Mater. 31 (21) (2021), 2010609.
[5] M.I. Alvarez Echazu, O. Perna, C.E. Olivetti, P.E. Antezana, S. Municoy, M. V. Tuttolomondo, J.M. Galdopórpora, G.S. Alvarez, D.G. Olmedo, M.F. Desimone, Recent advances in synthetic and natural biomaterials-based therapy for bone defects, Macromol. Biosci. 22 (4) (2022), 2100383.
[6] M. Mirkhalaf, Y. Men, R. Wang, Y. No, H. Zreiqat, Personalized 3D printed bone scaffolds: a review, Acta Biomater. 156 (2023) 110–124.
[7] M. Janmohammadi, M.S. Nourbakhsh, Recent advances on 3D printing in hard and soft tissue engineering, Int. J. Polym. Mater. Polymeric Biomater. 69 (7) (2020) 449–466.
[8] M. Bahraminasab, Challenges on optimization of 3D-printed bone scaffolds, Biomed. Eng. Online 19 (1) (2020) 1–33.
[9] G. Turnbull, J. Clarke, F. Picard, P. Riches, L. Jia, F. Han, B. Li, W. Shu, 3D bioactive composite scaffolds for bone tissue engineering, Bioact. Mater. 3 (3) (2018) 278–314.
[10] Y. Chen, W. Li, C. Zhang, Z. Wu, J. Liu, Recent developments of biomaterials for additive manufacturing of bone scaffolds, Adv. Healthcare Mater. 9 (23) (2020), 2000724.
[11] D. Gupta, A.K. Singh, N. Kar, A. Dravid, J. Bellare, Modelling and optimization of NaOH-etched 3-D printed PCL for enhanced cellular attachment and growth with minimal loss of mechanical strength, Mater. Sci. Eng. C 98 (2019) 602–611.
[12] M. Janmohammadi, M.S. Nourbakhsh, M. Bahraminasab, L. Tayebi, Effect of pore characteristics and alkali treatment on the physicochemical and biological properties of a 3D-printed polycaprolactone bone scaffold, ACS Omega 8 (8) (2023) 7378–7394.
[13] J. Sonatkar, B. Kandasubramanian, Bioactive glass with biocompatible polymers for bone applications, Eur. Polym. J. 160 (2021), 110801.
[14] R. Kumar, I. Pattanayak, P.A. Dash, S. Mohanty, Bioceramics: a review on design concepts toward tailor-made (multi)-functional materials for tissue engineering applications, J. Mater. Sci. 58 (8) (2023) 3460–3484.
[15] R. De Santis, V. Guarino, L. Ambrosio, Composite Biomaterials for Bone Repair , Bone repair biomaterials, Elsevier2019, pp. 273-299.
[16] Z. Nazemi, M. Sahraro, M. Janmohammadi, M.S. Nourbakhsh, H. Savoji, A review on tragacanth gum: a promising natural polysaccharide in drug delivery and cell therapy, Int. J. Biol. Macromol. (2023), 124343.
[17] E.N. Zare, P. Makvandi, F.R. Tay, Recent progress in the industrial and biomedical applications of tragacanth gum: a review, Carbohydr. Polym. 212 (2019) 450–467.
[18] M.P. Nikolova, M.S. Chavali, Recent advances in biomaterials for 3D scaffolds: a review, Bioact. Mater. 4 (2019) 271–292.
[19] Y.C. Fredholm, N. Karpukhina, D.S. Brauer, J.R. Jones, R.V. Law, R.G. Hill, Influence of strontium for calcium substitution in bioactive glasses on degradation, ion release and apatite formation, J. R. Soc. Interface 9 (70) (2012) 880–889.
[20] N. Abbasi, S. Hamlet, R.M. Love, N.-T. Nguyen, Porous scaffolds for bone regeneration, J. Sci.: Adv. Mater. Devices 5 (1) (2020) 1–9.
[21] J. Wang, D. Wu, Z. Zhang, J. Li, Y. Shen, Z. Wang, Y. Li, Z.-Y. Zhang, J. Sun, Biomimetically ornamented rapid prototyping fabrication of an apatite–collagen–polycaprolactone composite construct with nano–micro–macro hierarchical structure for large bone defect treatment, ACS Appl. Mater. Interfaces 7 (47) (2015) 26244–26256.
[22] A. Rashad, S. Mohamed-Ahmed, M. Ojansivu, K. Berstad, M.A. Yassin, T. Kivijärvi, E.B. Heggset, K. Syverud, K. Mustafa, Coating 3D printed polycaprolactone scaffolds with nanocellulose promotes growth and differentiation of mesenchymal stem cells, Biomacromolecules 19 (11) (2018) 4307–4319.
[23] M. Bahraminasab, N. Doostmohammadi, A. Talebi, S. Arab, A. Alizadeh, A. Ghanbari, A. Salati, 3D printed polylactic acid/gelatin-nano-hydroxyapatite/platelet-rich plasma scaffold for critical-sized skull defect regeneration, Biomed. Eng. Online 21 (1) (2022) 1–25.
[24] S. Hesaraki, M. Nouri-Felekori, N. Nezafati, S. Borhan, Preparation, characterization, and in vitro biological performance of novel porous GPTMS-coupled tragacanth/nano-bioactive glass bone tissue scaffolds, Mater. Today Commun. 27 (2021), 102335.
[25] L. Souza, J.H. Lopes, D. Encarnação, I.O. Mazali, R.A. Martin, J.A. Camilli, C. A. Bertran, Comprehensive in vitro and in vivo studies of novel melt-derived Nb-substituted 45S5 bioglass reveal its enhanced bioactive properties for bone healing, Sci. Rep. 8 (1) (2018), 12808.
[26] S. Manafi, F. Mirjalili, R. Reshadi, Synthesis and evaluation of the bioactivity of fluorapatite–45S5 bioactive glass nanocomposite, Progress Biomater. 8 (2) (2019) 77–89.
[27] T. Ghassemi, A. Shahroodi, M.H. Ebrahimzadeh, A. Mousavian, J. Movaffagh, A. Moradi, Current concepts in scaffolding for bone tissue engineering, Arch. Bone Joint Surg. 6 (2) (2018) 90.
[28] C. Bossard, H. Granel, Y. Wittrant, É. Jallot, J. Lao, C. Vial, H. Tiainen, Polycaprolactone/bioactive glass hybrid scaffolds for bone regeneration, Biomed. Glasses 4 (1) (2018) 108–122.
[29] M. Shaltooki, G. Dini, M. Mehdikhani, Fabrication of chitosan-coated porous polycaprolactone/strontium-substituted bioactive glass nanocomposite scaffold for bone tissue engineering, Mater. Sci. Eng. C 105 (2019), 110138.
[30] C. Wang, W. Huang, Y. Zhou, L. He, Z. He, Z. Chen, X. He, S. Tian, J. Liao, B. Lu, 3D printing of bone tissue engineering scaffolds, Bioact. Mater. 5 (1) (2020) 82–91.
[31] P.S. Poh, D.W. Hutmacher, B.M. Holzapfel, A.K. Solanki, M.M. Stevens, M. A. Woodruff, In vitro and in vivo bone formation potential of surface calcium

phosphate-coated polycaprolactone and polycaprolactone/bioactive glass composite scaffolds, Acta Biomater. 30 (2016) 319–333.
[32] H.D. Kim, S. Amirthalingam, S.L. Kim, S.S. Lee, J. Rangasamy, N.S. Hwang, Biomimetic materials and fabrication approaches for bone tissue engineering, Adv. Healthcare Mater. 6 (23) (2017), 1700612.
[33] S. Ruijtenberg, S. van den Heuvel, Coordinating cell proliferation and differentiation: antagonism between cell cycle regulators and cell type-specific gene expression, Cell Cycle 15 (2) (2016) 196–212.
[34] Y. Deng, X. Liu, A. Xu, L. Wang, Z. Luo, Y. Zheng, F. Deng, J. Wei, Z. Tang, S. Wei, Effect of surface roughness on osteogenesis in vitro and osseointegration in vivo of carbon fiber-reinforced polyetheretherketone–nanohydroxyapatite composite, Int. J. Nanomed. 10 (2015) 1425.
[35] O.A. Tarazona, O. Pourquie, Exploring the influence of cell metabolism on cell fate through protein post-translational modifications, Dev. Cell 54 (2) (2020) 282–292.
[36] T.S. Cliff, S. Dalton, Metabolic switching and cell fate decisions: implications for pluripotency, reprogramming and development, Curr. Opin. Genet. Dev. 46 (2017) 44–49.
[37] M. Rasti, S. Hesaraki, N. Nezafati, Effects of GPTMS concentration and powder to liquid ratio on the flowability and biodegradation behaviors of 45S5 bioglass/tragacanth bioactive composite pastes, J. Appl. Polym. Sci. 136 (22) (2019), 47604.
[38] J. Ru, Q. Wei, L. Yang, J. Qin, L. Tang, J. Wei, L. Guo, Y. Niu, Zein regulating apatite mineralization, degradability, in vitro cells responses and in vivo osteogenesis of 3D-printed scaffold of n-MS/ZN/PCL ternary composite, RSC Adv. 8 (34) (2018) 18745–18756.
[39] L. Xia, W. Ma, Y. Zhou, Z. Gui, A. Yao, D. Wang, A. Takemura, M. Uemura, K. Lin, Y. Xu, Stimulatory effects of boron containing bioactive glass on osteogenesis and angiogenesis of polycaprolactone: in vitro study, BioMed Res. Int. 2019 (2019).
[40] M.P. Bernardo, B.C. da Silva, A.E. Hamouda, M.A. de Toledo, C. Schalla, S. Rütten, R. Goetzke, L.H. Mattoso, M. Zenke, A. Sechi, PLA/Hydroxyapatite scaffolds exhibit in vitro immunological inertness and promote robust osteogenic differentiation of human mesenchymal stem cells without osteogenic stimuli, Sci. Rep. 12 (1) (2022) 2333.
[41] G. Calabrese, R. Giuffrida, C. Fabbi, E. Figallo, D. Lo Furno, R. Gulino, C. Colarossi, F. Fullone, R. Giuffrida, R. Parenti, Collagen-hydroxyapatite scaffolds induce human adipose derived stem cells osteogenic differentiation in vitro, PLoS One 11 (3) (2016), e0151181.
[42] M. Dziadek, K. Dziadek, K. Checinska, B. Zagrajczuk, M. Golda-Cepa, M. Brzychczy-Wloch, E. Menaszek, A. Kopec, K. Cholewa-Kowalska, PCL and PCL/bioactive glass biomaterials as carriers for biologically active polyphenolic compounds: comprehensive physicochemical and biological evaluation, Bioact. Mater. 6 (6) (2021) 1811–1826.
[43] F.V. Ferreira, L.P. Souza, T.M. Martins, J.H. Lopes, B.D. Mattos, M. Mariano, I. F. Pinheiro, T.M. Valverde, S. Livi, J.A. Camilli, Nanocellulose/bioactive glass cryogels as scaffolds for bone regeneration, Nanoscale 11 (42) (2019) 19842–19849.
[44] Q. Chen, R.P. Garcia, J. Munoz, U. Pérez de Larraya, N. Garmendia, Q. Yao, A. R. Boccaccini, Cellulose Nanocrystals bioactive glass hybrid coating as bone substitutes by electrophoretic Co-deposition: in situ control of mineralization of bioactive glass and enhancement of osteoblastic performance, ACS Appl. Mater. Interfaces 7 (44) (2015) 24715–24725.
[45] M. Neufurth, X. Wang, S. Wang, R. Steffen, M. Ackermann, N.D. Haep, H. C. Schröder, W.E. Müller, 3D printing of hybrid biomaterials for bone tissue engineering: calcium-polyphosphate microparticles encapsulated by polycaprolactone, Acta Biomater. 64 (2017) 377–388.
[46] X. Feng, L. Ma, H. Liang, X. Liu, J. Lei, W. Li, K. Wang, Y. Song, B. Wang, G. Li, Osteointegration of 3D-printed fully porous polyetheretherketone scaffolds with different pore sizes, ACS Omega 5 (41) (2020) 26655–26666.